



PAPER

OPEN ACCESS

RECEIVED
25 October 2023REVISED
21 December 2023ACCEPTED FOR PUBLICATION
28 December 2023PUBLISHED
10 January 2024

Original content from this work may be used under the terms of the [Creative Commons Attribution 4.0 licence](#).

Any further distribution of this work must maintain attribution to the author(s) and the title of the work, journal citation and DOI.



Quantum tunnelling in hafnia-based metal-insulator-metal diodes: atomistic-to-continuum modelling approach and experimental validation

Eleonora Pavoni¹ , Emiliano Laudadio¹ , Christopher Hardly Joseph² , Gian Marco Zampa² , Paola Russo² , Elaheh Mohebbi¹, Davide Mencarelli² , Mircea Dragoman³ , Pierluigi Stipa¹ , Luca Pierantoni² and Martino Aldrigo^{3,*}

¹ Department of Science and Engineering of Matter, Environment and Urban Planning, Marche Polytechnic University, Via Brecce Bianche, 60131 Ancona, Italy

² Department of Information Engineering, Marche Polytechnic University, Via Brecce Bianche, 60131 Ancona, Italy

³ National Institute for Research and Development in Microtechnologies, IMT-Bucharest, 077190 Voluntari (Ilfov), Romania

* Author to whom any correspondence should be addressed.

E-mail: martino.aldrigo@gmail.com

Keywords: density functional theory, hafnium oxide, metal-insulator-metal diode, modelling, simulation

Abstract

In this work, we present a metal-insulator-metal (MIM) diode, based on quantum tunnelling phenomena. Its model is based on a multilevel modelling approach consisting of atomistic and continuum simulations, fully validated by extensive measurements. The MIM structure comprises a hafnium oxide (or hafnia, HfO₂) dielectric layer, less than 4 nm thick and a square contact area of only 4 μm², placed between two metallic electrodes, namely platinum as the source and titanium as the drain. The current–voltage (I–V) curve has been estimated by Density Functional Theory (DFT) calculations through an optimisation of the interfaces between metals and monoclinic HfO₂. The dielectric parameters arising from *ab initio* computations have then been used as inputs for the successive circuit and electromagnetic simulations. Finally, the multilevel model has been validated with great accuracy, first measuring the I–V characteristics by applying a drain-source voltage between –1 V and +1 V, and then extracting the scattering parameters up to 40 GHz, thus demonstrating that DFT and circuit/electromagnetic simulations match almost perfectly the experimental ones. These outcomes represent the first study of such nanoscale devices investigated by means of a rigorous atomistic-to-continuum approach, providing invaluable information in order to improve fabrication and correctly assess the macroscale performance of nanoelectronics systems.

1. Introduction

Nowadays, the exploitation of new and environmentally friendly energy resources represents one of the most important challenges for the health of the planet. In particular, the improvement, development, and exploitation of environment-safe renewable energy, to supply low-power devices and components, are all together an important concept and one of the main objectives in many different research fields. In this context, radio frequency (RF) energy-harvesting and wireless power transfer (WPT) offer tangible opportunities to be taken into consideration, for remotely power wireless systems, such as small dust [1] or implantable [2] sensors. Collecting (‘harvesting’) RF signals regards the need to ‘recycle’ the otherwise lost RF energy generated by the radio environment and exploit it in low-voltage electronic devices. The RF radiation is scavenged and subsequently used to supply electronic devices. In this way, a new generation of battery free devices could be conceived, that is of fundamental importance to reduce battery waste.

In this context, diodes are mandatory to rectify the collected RF signal and generate direct current (DC) output voltage. In addition, these systems could be integrated with antennas to create the so-called rectennas [3].

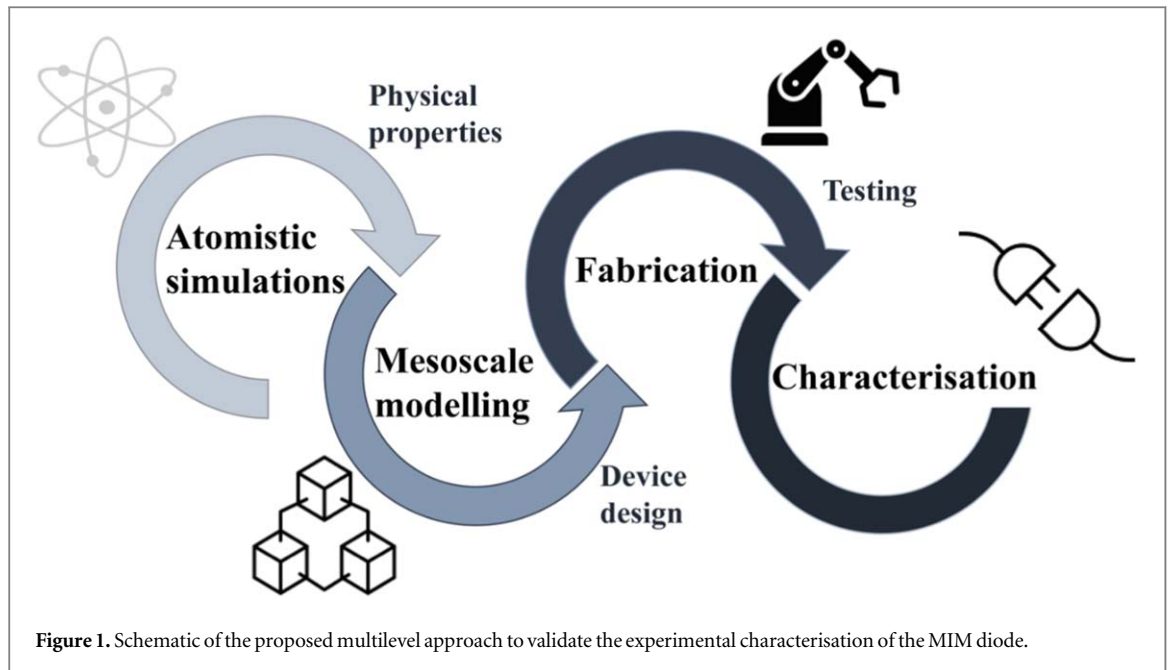
The metal-insulator-metal (MIM) diodes, whose working principle is based on the tunnelling effect, are particularly appealing for high-frequency applications. As a matter of fact, at high frequencies, the typical semiconductor-based devices cannot operate [4], while MIM diodes exhibit fast response times (in the order of a few femtoseconds) and have low-cost manufacturing and additive technologies for production [5]. Moreover, other great advantages are related to the capability of the MIM diodes to achieve cut-off frequencies in the THz range and to their ability of zero-bias rectification, particularly useful for WPT and energy-harvesting applications from RF [6] up to hundreds of GHz. From this perspective, it is essential to characterise MIM diodes in a wide range of frequencies. In order to accurately compute mismatch losses and combine MIM diodes with RF components with proper matching, RF characterisation of MIM diodes by means of scattering (S-) parameter measurements for impedance performance is crucial [7]. However, due to their intrinsic physical working principle, the bottleneck of MIM diodes is mostly connected with their fabrication, which requires an ultra-thin insulator layer embedded into a vertical stack, posing serious repeatability and reliability problems. In fact, the physical principle at the basis of MIM diodes is the tunnelling effect, where electrons cross the insulator layer, positioned between two metallic electrodes, thus the insulator layer must be thin enough (i.e., in the order of a few nanometres) to allow electrons to tunnel through. In other words, downsizing to the nanoscale dimension is fundamental to this technology.

The production of fast-response MIM devices represents a key point for many nanoelectronics applications, and at the same time is extremely sensitive to the nanoscale structural and chemical quality of interface regions; Dudek *et al* [8] used different growing techniques to prepare thin HfO₂ films on TiN electrodes, and then investigated the charge transport mechanisms of the HfO₂-based MIM diodes. El Kamel *et al* [9] studied the influence of the nature of metal electrodes, at different temperatures, on the conduction mechanisms of HfO₂-based MIM devices; in particular, they calculated the barrier heights at the metal-HfO₂ interfaces, by considering Al, Cr, and Au metal electrodes. Mitrovic *et al* [10] presented a review of MIM diodes considering a few crucial points, such as zero-bias responsivity, zero-bias dynamic resistance, and asymmetry. In the same work, even HfO₂ was considered as oxide for MIⁿM devices, summarising the electron affinity, bandgap, and permittivity; skin depths and work-function characteristics of some typical metal electrodes, among them Ni, Al, Au, Cr, and Ti, were also described.

Since the introduction by Intel in a manufacturing process in 2007, HfO₂ is nowadays used as high- κ material, thus revealing a full CMOS (complementary metal-oxide-semiconductor) compatibility. HfO₂ has a relatively wide bandgap (5.6 eV) [11], large band offset with Si, i.e., less parasitic leakage, large coercive field (at least 1 MV cm⁻¹), and medium-high permittivity. Moreover, the absence of an interfacial dead layer in HfO₂ makes this material a promising candidate in thin-film technology, unlike perovskites-based material, and the mid-range dielectric constant allows the switching at reasonable voltage values [12–15].

It is known that HfO₂ can adopt different crystal structures in the solid state, and the related chemical-physical properties accordingly change [16]; among the possible polymorphs, the monoclinic structure, with space group *P2₁/c*, is known to be the most stable one [16, 17].

Understanding the behavior of the involved physical phenomena from the atomistic point of view could be of great interest and of great impact on materials science and nanotechnology engineering. The use of *ab initio* simulations in order to predict the current–voltage (I–V) characteristic of a MIM diode is rarely reported in the literature because of the complexity of the required work and because just a few software tools allow to apply the quantum mechanical approach to a configuration suitable for the simulation of devices at the atomistic level. Previously, a DFT computation approach was used to calculate the I–V curve of a diode based on HfO₂ as the insulator layer [18] between platinum and gold metal electrodes. In detail, [18] focused only on the DFT modelling of different hafnia polymorphs and on the interface effects at the simulation level. On the contrary, the present study is centred around a real geometry and material stack for the MIM device, concentrating only on dielectric hafnia and providing, *for the first time*, a full modelling-simulation-experimental verification based on a rigorous description of quantum tunnelling phenomena. Al-Dirini *et al* [19] showed a class of nanoscale devices based on graphene monolayer in MISFEDs (Metal–Insulator–Semiconductor Field–Effect Diodes) configuration: in detail, they presented devices with excellent current–voltage characteristics that were also characterised by quantum mechanical simulations based on the Extended Huckel method and Nonequilibrium Green’s Function Formalism. Kang *et al* [20] reported a study of metal-TMD (transition-metal dichalcogenides) contacts by *ab initio* DFT calculations, for CMOS technology applications, by considering contacts between Au, Pd, In, or Ti, and monolayers of MoS₂ or WSe₂, and described the optimised geometries, partial density of states, electron densities, and effective potentials. Among the side contacts, the author found the best contact between MoS₂ and Ti, while for WSe₂ the most suitable one was with Pd. Gong *et al* [21] used the DFT calculations to understand the nature of the contact between metal electrodes and monolayer MoS₂ pointing particular attention to Schottky barriers and the Fermi level pinning mechanism. A paper from Yoshizawa *et al* [22] reported the DFT characterisation of the electron transport properties in molecular junctions, in which two electrodes had weak contact with a highly conjugated molecule, in terms of the HOMO–LUMO orbital.



In this paper, we aim at going beyond the actual state-of-the-art by presenting a comprehensive and multilevel modelling of a MIM diode, which consists of a dielectric layer of HfO_2 (with a thickness between 3 and 4 nm) between two different metals, i.e., platinum (Pt) and titanium (Ti), which are the source and drain electrodes, respectively. The contact area of the Pt- HfO_2 -Ti structure is squared-shaped with edges of $2 \mu\text{m}$ (i.e., with a total contact area of $4 \mu\text{m}^2$).

First, the MIM device was simulated using an *ab initio* DFT approach to provide an in-depth insight into MIM diode's structure and conduction mechanism. Then, an electromagnetic (EM) high-frequency model has been developed using the outcomes of the DFT calculations. This means that *ab initio* simulations give not only the characterisation of the device but also assist the EM modelling by providing the parameter to be used, e.g., the dielectric constant and conductivity of the material at different frequencies. The proposed method exhibits the best balance between accuracy and reasonable computational time, considering that *ab initio* simulations are very cumbersome, since they do not take advantage of any *a priori* fitted parameters. After that, the MIM diode has been fabricated and measured to validate the multilevel modelling approach. Making use of atomic layer deposition (ALD) techniques and a state-of-the-art process to create the bridge for the top electrode, tens of devices have been created on a high-resistivity silicon (HRSi) 4-inch wafer in a coplanar waveguide (CPW) technology. The latter choice was dictated by the necessity of having a reliable on-wafer characterisation using standard probe tips. Finally, we performed detailed DC and RF measurements to fully assess the electrical performance of the diodes. As reported in figure 1, the overview of the proposed approach regards a combination of theoretical and experimental work interconnected and with mutual verification. To the authors' knowledge, this is the first computational platform aimed at simulating MIM diodes, through the seamless integration of atomistic- with mesoscale-level computational tools. The former (atomistic), starting from the atomic structure of the nanoscale material, provides and transfer phenomenological parameters/equations (e.g., constitutive relations) to the latter, thus allowing the correct assessment of the electromagnetic propagation in the final device.

The manuscript is structured as follows: before focusing on the entire device, an accurate overview of the optical and electronic properties of monoclinic HfO_2 is provided using DFT computations. The bulk properties calculated with this method have been compared with the data already reported in the literature [16, 23, 24]. Afterwards, Pt and Ti electrodes have been considered separately and the interfaces with monoclinic HfO_2 were optimised using the DFT-D3 approach [25]. In such complex systems, the optimisation of the interface between the electrodes and the oxide layer plays a key role: in fact, the phenomena characterising the electrical properties of nanoscale devices are strongly dependent on the interface implementation. More in detail, the transitions and the bonding characters at metal-oxide edges, and the different electronic structures of both the metals and HfO_2 are fundamental to understand how they are coupled at the interface. Moreover, Pt and Ti electrodes could be described by diverse Miller indices, thus generating different possible interaction patterns. In this respect, for this work the (100) Miller configurations have been chosen for both metal types, since these are the most stable configurations apt to generate interfaces [26, 27]. After this step, the optimised metal- HfO_2 interfaces were used to model the entire MIM device, then the I-V curve was properly calculated, as well as the dielectric constant and

conductivity necessary to electromagnetically characterise the diode. Regarding the latter issue, the MIM diode has been modelled as a lossy capacitive element inserted in series with a CPW line. The dielectric parameters used to model the MIM device have been taken from the atomistic characterisation, as well as from the simulated I–V characteristics. Then, details of the fabrication of the hafnia-based MIM diodes are provided. The geometrical, optical, and electronic properties of monoclinic HfO₂ serve as the basis for the assessment of the metal–HfO₂ interfaces and I–V characteristics, which represent the preliminary step for the circuit and EM simulations. Finally, an accurate experimental characterisation and a thorough comparison with the multilevel modelling is offered, thus confirming the correctness of the latter and overcoming the problem of translating nanoscale phenomena into meso- and macroscale observations.

2. Method

2.1. Theoretical background

The physical principle on which a MIM diode relies is the quantum tunnelling of electrons, and this phenomenon occurs in about 10^{-12} – 10^{-15} s, thus enabling ultra-fast devices with high cut-off frequency. One needs to consider that the tunnelling probability falls exponentially as a function of insulator's thickness and electrons can be emitted above the barrier also due to thermal excitation. Nonlinearity and asymmetry can be increased by using different metals for the electrodes (hence, metals with dissimilar work-functions—the bigger the difference, the bigger the nonlinearity and asymmetry) and multiple thin insulators, sometimes also interposing intermediate metallic layers. Unfortunately, the latter solution is challenging from the technological point of view and expensive if one aims at enhancing electron tunnelling at low power levels. The physical equations governing the quantum tunnelling in a MIM diode provide (with a reasonable approximation) the total current density J_{MIM} that accounts for two main contributions: (1) the thermionic emission-limited current J_{th} and (2) the tunnel-limited current J_{tun} , which can also include the image force impact on the potential barrier in the so-called ‘composite Simmons model’ that is described as follows (more details can be found in [28]):

$$J_{th} = A_{th} T^2 e^{-\varphi_0/k_B T} (1 - e^{-qV/k_B T}) \quad (1)$$

$$J_{tun} = J_0 \left[\Phi e^{-A_{tun} \sqrt{\Phi}} - (\Phi + qV) e^{-A_{tun} \sqrt{\Phi + qV}} \right] \quad (2)$$

$$J_{tot} = J_{th} + J_{tun}. \quad (3)$$

where $A_{th} = 4\pi m q k_B^2 / h^3$ is Richardson's thermal constant, $J_0 = q / [2\pi h (\alpha \Delta s)^2]$, $A_{tun} = (4\pi \alpha \Delta s / h) \sqrt{2m}$, and $\Phi = \frac{1}{\Delta s} \int_{s_1}^{s_2} \varphi(x) dx$. We stress here that the total potential in the insulator is given by $V_{tot} = \varphi(x) + (-0.288t) / [\varepsilon x(t-x)]$, where $\varphi(x)$ is the potential energy between the electrodes, x identifies the position inside the insulator, ε is insulator's permittivity, and t is insulator's thickness. V_{tot} takes into account the image potential between the two electrodes, which has a significant impact on the accurate modelling of J_{th} , as it lowers the potential barrier. However, this mathematical approach does not consider the metal–insulator interface phenomena, as well as defect assisted tunnelling in the insulator. Hence, a DFT simulation approach has been deployed to better describe the quantum tunnelling in hafnia-based MIM diodes, thus providing an accurate estimation of the macroscopic performance, as explained in the following.

2.2. DFT simulations

All simulations were performed using the DFT methodology. Specifically, by means of Quantum Atomistic Toolkit (Q-ATK) we simulated the HfO₂ properties and the I–V characteristics [29] by making use of the Perdew–Burke–Ernzerhof (PBE) [30] general gradient approximation (GGA) [31] density functional for the electron exchange–correlation (xc) energy, in combination with norm-conserving (NC) PseudoDojo [32] pseudopotentials for the description of the core electrons of each atom. Pt and Ti metals have been considered separately during the formation of the interfaces with monoclinic HfO₂, and then they have been optimised using DFT-D3 [33] through QuantumEspresso (QE) [34].

To calculate the geometrical parameters, the optical, and the electronic properties of monoclinic ($P2_1/c$) HfO₂, the periodic boundary conditions (PBC) have been applied to all the three x , y , and z axes, to avoid complications produced by the finite size and to moderate the calculation time while maintaining a high accuracy. The energy cut-off used in the calculations was 1200 eV, and the Brillouin-zone integration was performed using a $15 \times 15 \times 15$ k -points grid. These parameters were chosen to ensure the total energy convergence of 5.0×10^{-6} eV/atom, a maximum stress of 2.0×10^{-2} GPa, and a maximum displacement of 5.0×10^{-4} Å. The linear combination of the atomic orbital (LCAO) methodology has been used as electron basis set for Hf and O entities [35]. The $5d^2$ and $6s^2$ electrons of Hf and $2s^2$ and $2p^4$ electrons of O have been explicitly

treated as valence. Correct on-site repulsion values have been calibrated, then the Hubbard (U) values of 5.8 eV and 4 eV for Hf^d and O^p valence electrons have been chosen, respectively, to better treat the chemical bonds in which d electrons are involved. When U values are included, the description of the charge density of the core region could overlap with valence density; hence, the choice of the correct NC PDj becomes very important. As a matter of fact, the charge density of the electron core has been reproduced within a short cut-off radius, thus avoiding an underestimation of the xc energy.

The interfaces between HfO_2 and the two Pt and Ti metals, both with a Miller index (100), have been built and optimised using QE. To study the interfaces that HfO_2 creates with both metals, the single-particle wave functions have been expanded on a basis of plane-wave (PW) functions, and D3 corrective terms have been added using PBCs along x and y axes. In particular, the corrective three-dimensional term D3 is essential to consider the phenomena at the material interfaces, both as short- and long-range interactions. Additionally, the boundary condition on the z -axis cannot be periodic, since this constitutes a semi-finite model, so that it will be assumed by the Dirichlet method, which allows the generation of two gradient potentials on the two sides of the box, in order to reproduce the extension of each material type (i.e., HfO_2 in one direction and Pt or Ti along the other). With this approach, the interfaces have been optimised and then they have been used to model the entire device system.

To simulate the I–V curve, PBCs have been used along the x and y axes, while the gradient potential has been generated along the z -axis using Dirichlet conditions to simulate the Ti and Pt on the opposite sides of the simulation box. The electronic transport properties have been calculated using the Nonequilibrium Green's Function (NEGF) formalism [34]. The device structure consists of three regions: the source, the central region, and the drain. A coherent transport of electrons has been assumed to occur between the source and drain contacts, with Fermi levels m_S and m_D (and vice versa) passing through the central HfO_2 region. According to the Landauer formula, the coherent current between the electrodes is given by equation (4):

$$I(V) = \frac{2e}{h} \int_{\mu_S}^{\mu_D} T(E, V) [f_0(E - \mu_D) - f_0(E - \mu_S)] dE \quad (4)$$

where $T(E, V)$ is the transmission probability of incident electrons with energy E from the drain (D) to source (S), $f_0(E - m_{S(D)})$ is the Fermi–Dirac distribution function of electrons in the source, and drain, respectively, and $V = (m_S - m_D)/e$ is the potential difference between source and drain.

2.3. Circuit level and full-wave electromagnetic simulations

To estimate the behavior of the device at high frequencies, the MIM diode was placed in series with a planar transmission line such as CPW. The CPW can be modelled, in principle, as a transmission line where the MIM device model is inserted in series as shown in figure 2(a). The equivalent circuit of the MIM diode can be described as a parallel of a capacitance and a conductance/resistance connected in series to the transmission line as presented in the literature [36, 37].

The main contribution to the capacitance is given by the geometric one that can be simply calculated from equation (5). The conductance can be easily extrapolated by the I–V characteristics obtained from the atomistic simulations using equation (6).

$$C = \epsilon_0 \epsilon_r \frac{A}{d} \quad (5)$$

$$G(V) = \frac{\partial I}{\partial V} \quad (6)$$

In order to validate the model of the MIM device, it is necessary to realise an experimental setup based on the CPW, allowing a 50Ω characteristic impedance of the line, but at the same time able to integrate the MIM diode. For this reason, a modification of the CPW line is proposed in figure 2(b), where the detail of the MIM device integration is shown.

The CPW line is designed in such a way as to offer a characteristic impedance of 50Ω with the following specifications: the signal line width (w) is $100 \mu\text{m}$, the gap (g) is $60 \mu\text{m}$, and the total length (l) is $408 \mu\text{m}$. The line is placed on a substrate consisting of HRSi (with a thickness of $525 \mu\text{m}$), covered with a 300-nm-thick film of silicon dioxide (SiO_2). The circuit was optimised so as to present impedance matching up to 60 GHz.

The three-dimensional (3D) model of figure 2(b) was simulated using two different full-wave EM commercial solvers (i.e., COMSOL Multiphysics and CST Microwave Studio) to verify the accuracy of the modelled diode. Moreover, we compared the performance of the proposed setup with the transmission line-based theoretical model. The device analysed was subsequently fabricated and measured to validate the model. Results are shown and discussed in section (3). COMSOL Multiphysics can also be deployed to predict the hysteresis characteristics of a HfO_2 -based ferroelectric thin film (i.e., with a thickness of just a few nanometres), in which the ferroelectricity is induced either by oxygen vacancies or by some type of doping, e.g., using Zr, Y, S,

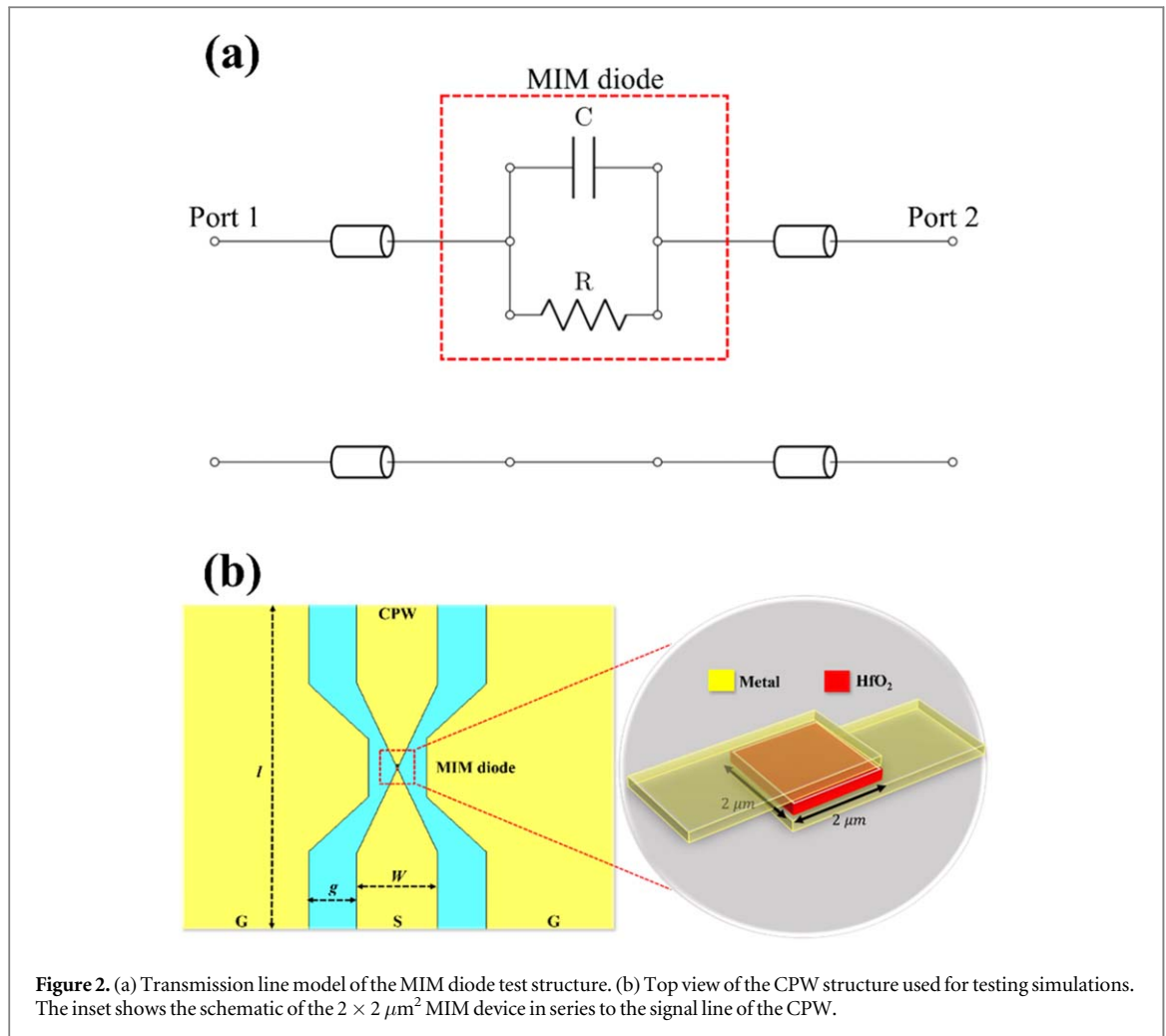


Figure 2. (a) Transmission line model of the MIM diode test structure. (b) Top view of the CPW structure used for testing simulations. The inset shows the schematic of the $2 \times 2 \mu\text{m}^2$ MIM device in series to the signal line of the CPW.

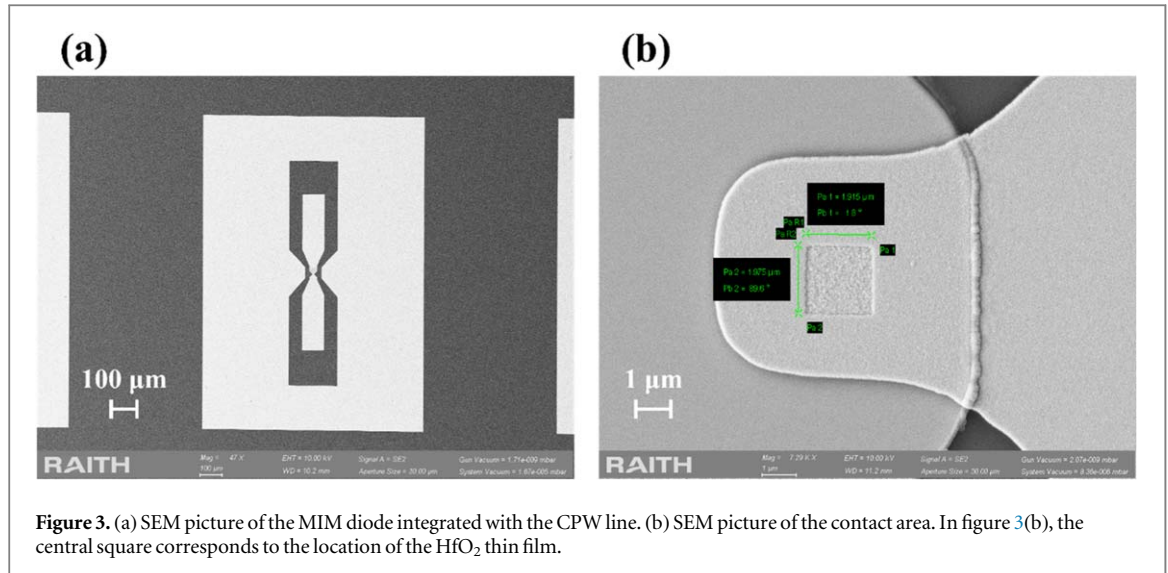
etc. In this case, the polarisation P can be computed from the Time-Dependent Landau-Ginzburg equation (TDLG) as in [38, 39], as follows:

$$-\Gamma \frac{\partial P}{\partial t} + k \nabla^2 P = \alpha P + \beta P^3 + \gamma P^5 - E \quad (7)$$

where Γ is the finite velocity of the polarisation switch giving rise to the hysteresis loop, k is the spatial variation of the polarisation (i.e., domain wall motion), α is the linear term of the response of the material, and E is the external electric field. Then, P is coupled with E using either the Poisson equation (for devices smaller than the considered wavelength) or Maxwell equations. In COMSOL Multiphysics, (7) can be coupled to Maxwell equations, which allows modelling the polarisation effects in ferroelectric thin films at high frequencies.

2.4. Fabrication

The fabrication of the HfO₂-based MIM diodes involved several steps, as described in [28]. Photolithography was used to define the Pt bottom electrode, and a 20-nm-thick chrome (Cr)/100-nm-thick Pt layer was deposited by e-gun evaporation onto the SiO₂/HRSi 4-inch wafer. The Cr layer was necessary for Pt adhesion to the substrate. Then, a 100-nm-thick Si₃N₄ layer was deposited by plasma enhanced chemical vapor deposition (PECVD) on the whole surface. The role of the Si₃N₄ was to create a mechanical support to create the bridge connecting MIM diode's top electrode to the CPW line, thus realising the proper vertical stack of a MIM structure and avoiding short-circuits with the bottom electrode. E-beam lithography and etching of Si₃N₄ using CF₄/O₂ plasma were used for defining the active area of the contact near the centre of the Si₃N₄ spacer. The ALD process of the less than 4-nm-thick HfO₂ thin film was carried out at 250 °C with Tetrakis(ethylmethanido)-hafnium (TEMAHf) as precursor and H₂O as oxidiser. The HfO₂ layer was patterned using Cl₂/BCl₃ plasma etching. The top electrode was defined by lift-off and evaporation of a 100-nm-thick Ti/200-nm-thick Au layer. As in the case of the Cr layer for the bottom electrode, here the Ti layer provides adhesion of the Au metallisation. At the same time, the proper MIM stack is of the type Pt-HfO₂-Ti (as was correctly stated before), not Pt-HfO₂-Au. It is very important to stress this point, as different metals possess different work-functions, which



can dramatically affect the performance of the device under test. Last, a 500-nm-thick Au layer was deposited to define the CPW structure and to provide the necessary thickness to overcome potential high-frequency skin depth effects. Figure 3 shows the scanning electron microscope (SEM) pictures of (a) a complete test structure (i.e., the MIM diode integrated with the CPW line) and (b) the MIM contact area. The final test devices have overall dimensions of just $1 \times 1.41 \text{ mm}^2$ and, as one can see in figure 3(a), the ground plane surrounds the two CPW lines embedding the MIM diode; this design strategy ensures the optimal electrical connections when measuring on-wafer the fabricated devices.

3. Results and discussion

3.1. Geometrical, optical, and electronic properties of monoclinic HfO₂

The lattice parameters for monoclinic HfO₂ were obtained by systematically changing the atomic positions and adjusting the size and angle of the unit cell until convergence was achieved. This optimisation process allowed us to obtain the most suitable parameters. As a result, the unit cell dimensions were found to be 5.068 Å, 5.135 Å, and 5.292 Å for a, b, and c, respectively, and these values were in good agreement with the literature [40]. The real part (ϵ_{real}) and imaginary part (ϵ_{im}) of the dielectric function of monoclinic HfO₂ were calculated over a wide-energy range (figure 4(b)). As reported, the ϵ_{real} value at 0 eV was 5.73, while the ϵ_{im} was in the order of 10^{-4} from 0 eV up to 4 eV, in agreement with other studies [15, 41].

The GGA-PBE method, which has been used to describe the geometrical parameters, is not consistent when studying the excited state properties; thus, the inclusion of corrective terms is necessary for the calculation of the partial density of states (PDOS) and bandgap energy. The qualitative improvement of electronic descriptions and the better characterisation of chemical bonds involving Hf and O atoms required on-site Coulomb interaction by adding Hubbard (U) terms. The Hf U^d and the O U^p values have been settled to 5.8 eV and 4 eV [15], and the energy bandgap acquired with such a methodology is 5.68 eV (figure 4(c)), in line with experimental results reported in the literature [42, 43]. The uses of GGA/PBE with U values approach has also been used to calculate the partial density of states (PDOS) (figure 4(d)), which showed two different contributions before and after the Fermi Level. In particular, the major contribution originates in the energy range between about -7.5 to -2 eV, that is, the valence band maximum (VBM), due to O 2^p orbitals, while in the energy range starting from about 2.2 eV upwards, the conduction band maximum (CBM) is mainly due to Hf 5^d orbitals.

The capability of the herein proposed DFT approach is also confirmed by the good agreement between the calculated dielectric functions (figure 4(b)) and the absorption spectra reported in the literature for the monoclinic HfO₂ [44]. As a matter of fact, the real part of the dielectric function (ϵ) defines the capability of the matter to interact with an electric field without absorbing energy, while the imaginary part of the dielectric function represents the ability of the matter to permanently absorb energy from a time-varying electric field. Both parameters are linked to the optical properties of HfO₂. This material exhibits the main light absorption between 100 nm and 300 nm, as confirmed by our calculated dielectric function. In fact, the imaginary part of this function shows the most pronounced interaction between 4 eV and 12 eV. Moreover, the highest light

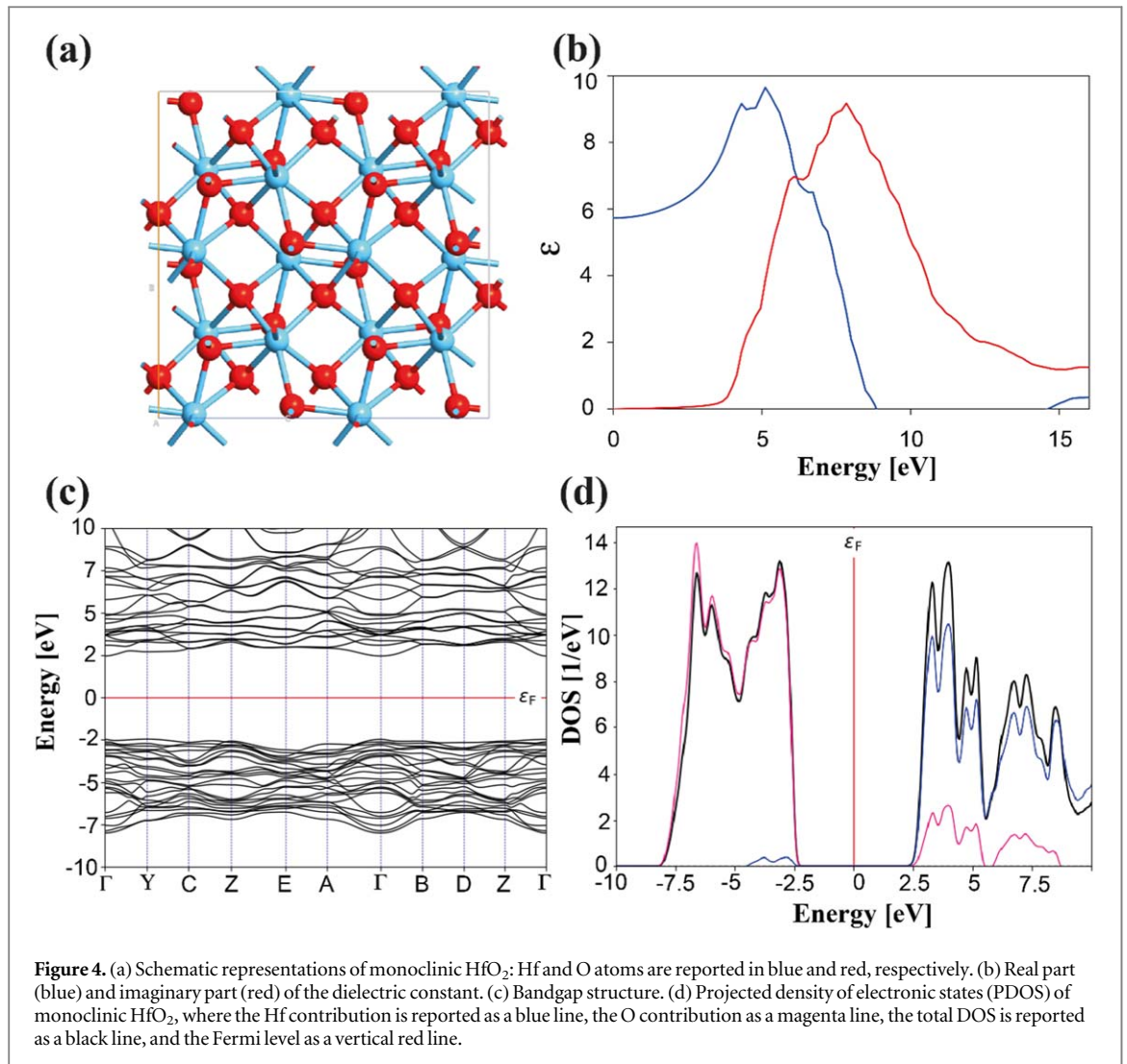


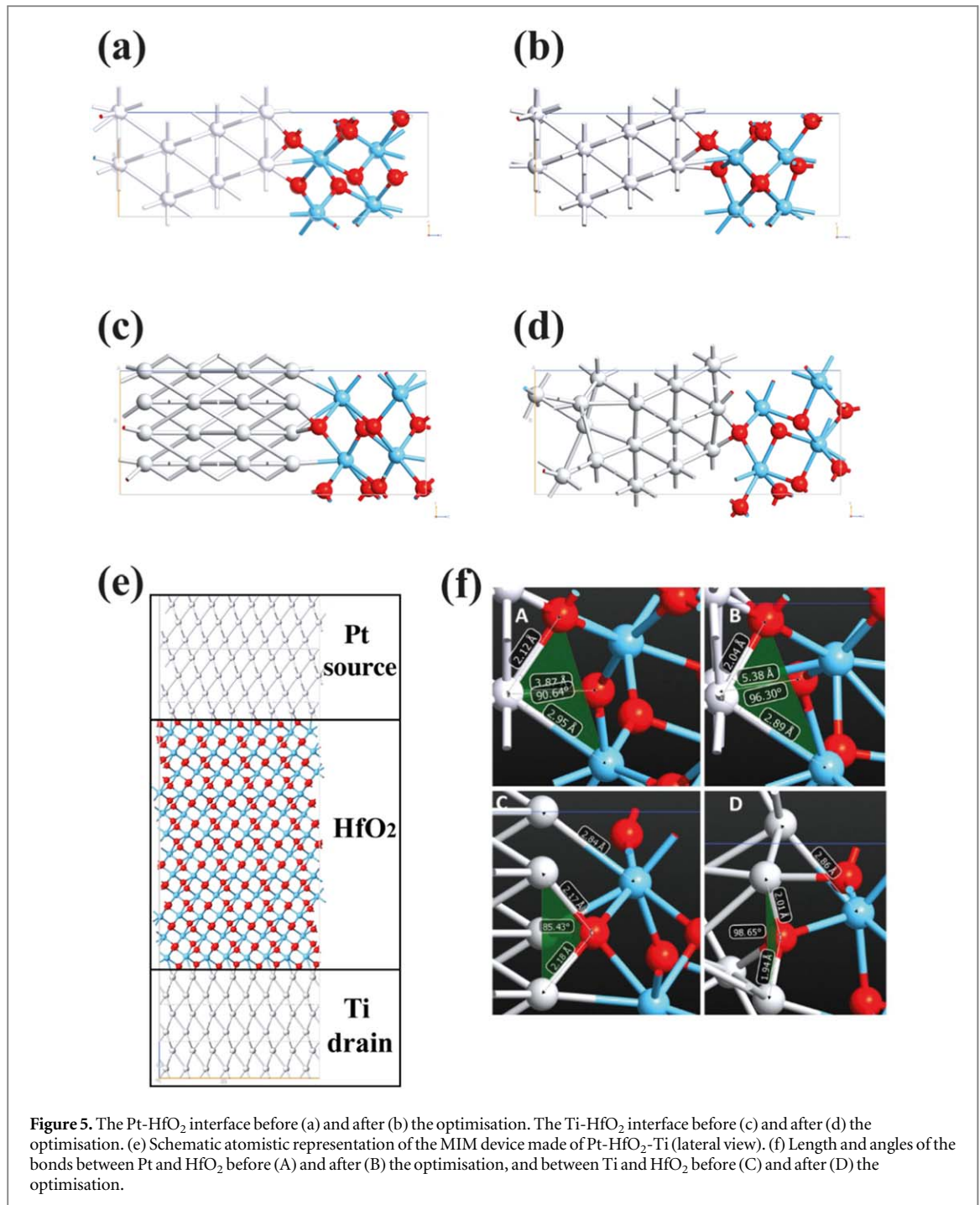
Figure 4. (a) Schematic representations of monoclinic HfO_2 ; Hf and O atoms are reported in blue and red, respectively. (b) Real part (blue) and imaginary part (red) of the dielectric constant. (c) Bandgap structure. (d) Projected density of electronic states (PDOS) of monoclinic HfO_2 , where the Hf contribution is reported as a blue line, the O contribution as a magenta line, the total DOS is reported as a black line, and the Fermi level as a vertical red line.

absorption is closely related to the bandgap energy, and for the monoclinic HfO_2 we found a bandgap of 5.68 eV that corresponds to about 220 nm.

As shown in figure 4(b), the calculated value for the real part of the dielectric constant was 5.73 at 0 GHz for the monoclinic bulk HfO_2 system. From an experimental point of view, the combination of amorphous microstructures with crystalline zones leads to an increased ionic polarisation mechanism, which is based on the high- κ behavior of this material. These results were in line with our predictions, then, in order to simulate the diode by means of a multilevel approach and to provide information to the EM modelling, the dielectric constant was estimated again, taking into account the monoclinic HfO_2 , with a thickness of 3.67 nm, as obtained after the geometrical optimisation and by excluding the metal interfaces; this approach has been chosen to investigate the dielectric behavior of the 3.67-nm-thick HfO_2 inserted between the metal electrodes. For this last system, the real part of the dielectric constant is 3.55 between 0 and 60 GHz. This decrease is not surprising, since the dielectric constant of such a material undergoes a dramatic reduction as the film thickness is decreased to a few nanometres [41]. The reason for this phenomenon is usually ascribed to the size effect, especially pronounced in ultra-thin film, and determined by the polarisation, which brings to a reduction of the effective dielectric constant; furthermore, this decrease is more remarkable for larger values of the bulk dielectric constant [45–47].

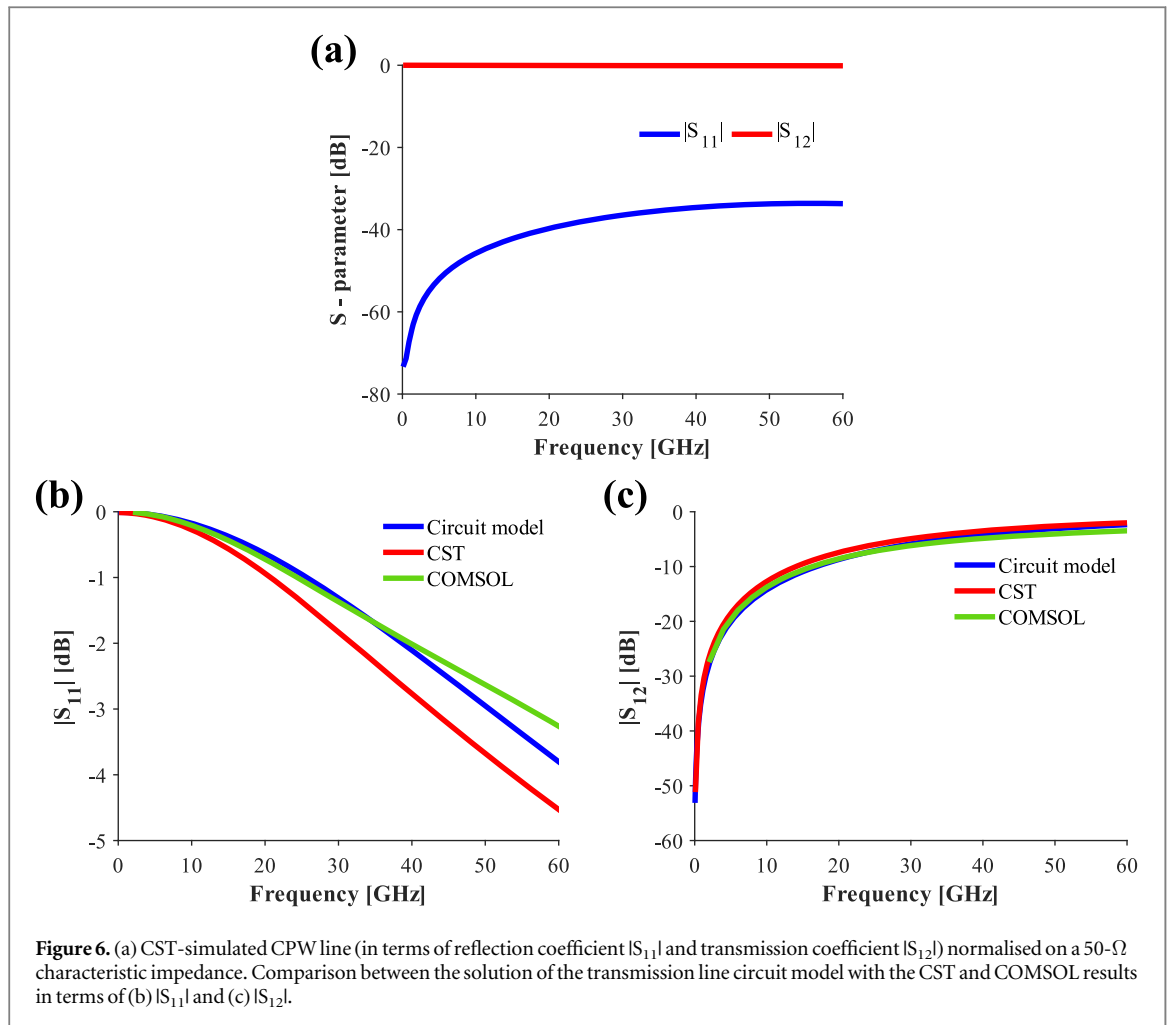
3.2. Metal- HfO_2 interfaces and I–V characteristics

The search for the most stable interfaces between different materials is crucial to maximise the performance of the MIM diode and to avoid artifacts; in order to achieve that, an extensive geometry optimisation of the interfaces was performed before the calculation of the I–V characteristics. As previously reported, both Ti and Pt atomic systems were considered with (100) Miller indices, and a 3.67-nm-thick monoclinic HfO_2 layer was interposed between the electrodes (figures 5(a)–(e)).



Before the device modelling, the cohesive formation energy of the optimised structures was calculated with a view to ensuring reliability of the obtained interfaces and securing reproduction of the same interfaces present in the real diode; indeed, such cohesive formation energy reports energy values, in eV per atom, considering the lengths and the angles of the bonds at the interface. After the optimisation step, the cohesive energy values resulted negative for both Pt-HfO₂ and Ti-HfO₂ systems, indicating the achievement of reliable and stable interfaces. More in detail, the Pt-HfO₂ system resulted to be the most stable one, with a calculated energy of -2.86 eV, while the Ti-HfO₂ interface was -2.23 eV. Such a small difference is strictly related to the electron configurations of Pt and Ti; Pt has nine valence *d* electrons accommodated in the 5th energy level, while Ti has only two *d* valence electrons placed in the 3rd level. Hence, the hybridisation of the atomic orbitals is different, and the resulting overlap of the wavefunctions for generating chemical bonds changes accordingly. Pt has a stronger adhesion if compared to Ti, because of the higher energy associated with its valence electrons.

To better clarify this aspect, the lengths and the angles of the bonds on the interfaces were measured before and after the energy optimisation (figure 5(f)). In both cases, an increase in the angle between oxygen, metal (Pt or Ti), and hafnium was detected as well as a decrease in the bonds between oxygen and metal (Pt or Ti). On the



other hand, in both the interfaces between Pt (100) or Ti (100) with HfO_2 , the distance between Hf and metal (Pt or Ti) atoms was not dissimilar to that of the starting structures. Despite the differences in cohesive energies caused by the electronic configurations of Pt and Ti, a univocal optimisation trend was detected for both systems, resulting in a reliable interface with HfO_2 . The modelled system was used as the starting point in assembling the complete MIM diode.

3.3. Electromagnetic simulations

The results of the atomistic model presented in the previous section were used as inputs for modelling the RF performance of the MIM diode as described in section (2).

Before analysing the MIM device, the proposed modification of the CPW line was tested to guarantee its match over a wide frequency range. For this reason, the MIM model was removed and substituted with a complete metallisation of the so-created gap. The scattering (S-) parameters of the line, normalised to 50 Ω , show much less reflection (S_{11} or S_{22}) and full transmission (S_{12} or S_{21}) up to 60 GHz, as shown in figure 6(a). This aspect is very important, as we need to detect the response of the MIM diode only, filtering out that of any mismatch arising from the CPW line.

The complete model of the structure, with the MIM device, was then simulated both with CST and COMSOL software. The input for the EM simulations of the HfO_2 layer considered a dielectric constant value of 3.55, as predicted by the atomistic simulations, and a conductivity of 0.01 S m^{-1} , as calculated from a differential resistance of 84 k Ω again estimated from the I-V curve of the MIM diode at the bias value of 0 V (see section (3.4)). This outcome is consistent with the typical differential resistance of a MIM device. The obtained results, between 1 and 60 GHz, are shown in figures 6(b)–(c), that also reports the results from the circuit model based on the transmission line theory (figure 2(a), section (2.3)). This comparison is necessary to be sure that the proposed setup does not introduce any higher-order modes that can modify the interpretation of the S-parameter results. The 3D-EM simulations are in good agreement with the results obtained from the circuit model, proving that the setup proposed is valid for the characterisation of the MIM structure only.

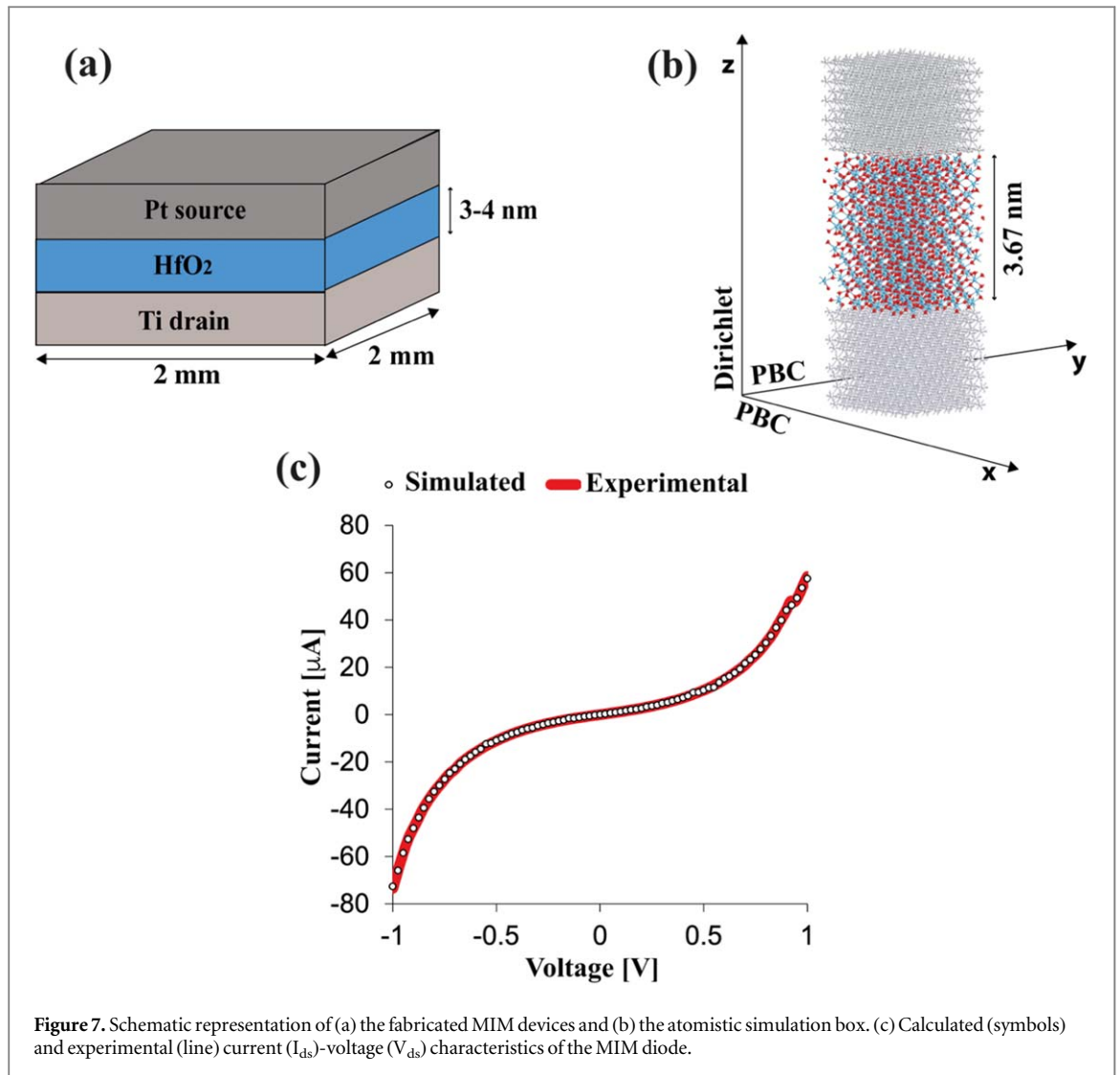
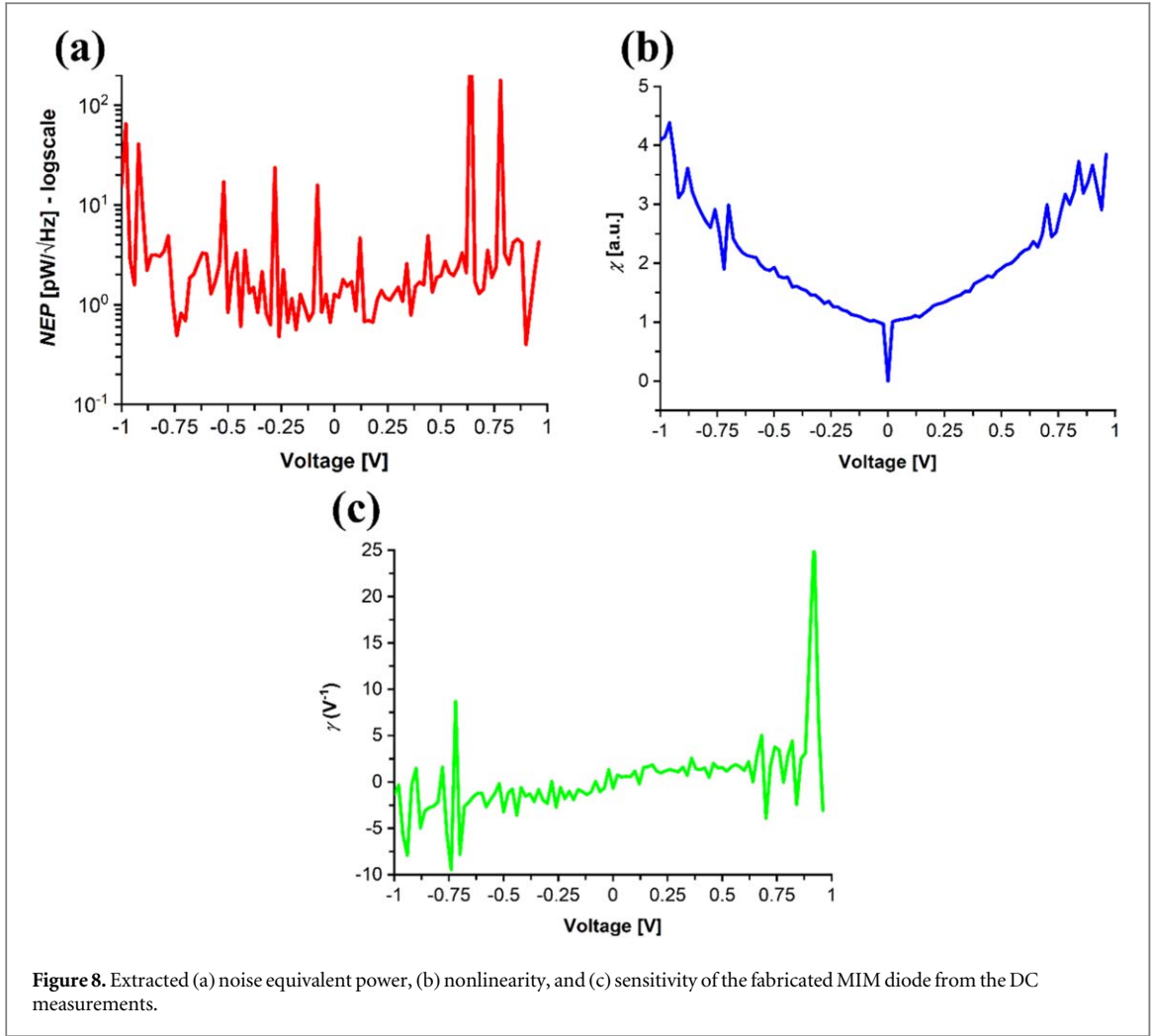


Figure 7. Schematic representation of (a) the fabricated MIM devices and (b) the atomistic simulation box. (c) Calculated (symbols) and experimental (line) current (I_{ds})-voltage (V_{ds}) characteristics of the MIM diode.

3.4. Experimental characterisation and comparison with the multilevel model

As already said, the proposed MIM diode can be schematised as a layered structure of Pt-HfO₂-Ti (figure 7(a)) in which the HfO₂ thickness is 3.67 nm and the contact area between the layers is 4 μm². In order to simulate such devices in a reasonable computational time by means of an atomistic algorithm, it is important to design the system accurately; hence, the dimensioning of the MIM device chosen to calculate the I-V curve was set to 2.88 nm, 2.62 nm, and 6.96 nm for the x, y, and z axes of the simulation box, respectively (figure 7(b)). Then, the I-V characteristics of the system was computed as described above, and the results are herein reported and compared with the experimental data (figure 7(c)). From the simulation point of view, the exact reproduction of the real dimensions of the device may require an impressive and impractical computational effort. To avoid such a huge computational cost, the PBC along the x and y axes were appropriately selected and applied by using a certain number of *k*-point samples, whereas the Dirichlet conditions were applied to the z-axis in order to maintain unaltered the layered structure of the MIM diode. In detail, to reproduce the I-V characteristics the contact area was simulated by applying 8 × 8 *k*-points to the x and y axes, while the Dirichlet condition was applied to the z-axis.

The curve obtained by *ab initio* simulations was calculated by applying a DC voltage bias, ranging between -1 V and +1 V, between the source and drain electrodes (V_{ds}), and the sampling in this interval was 81 points. The computational results were traced back to experimental measurements performed on the fabricated diode. The I-V curves, both theoretically estimated and experimentally measured, overlap completely, thus demonstrating the great capability of the proposed methodology to accurately describe the behavior of real MIM devices from an atomistic point of view. From the experimental data, we have also calculated a current density J greater than 3 A cm⁻². The electrical characterisation of the MIM diodes was performed on-wafer by means of a Keithley SCS 4200 station. The probe station for on-wafer measurements is placed inside a Faraday cage



connected to the station via low-noise amplifiers. Fitting algorithms were intentionally excluded during or after measurements, which were conducted at room temperature ($T = 290$ K).

The most important performance indicators of a MIM diode are the noise equivalent power NEP (in pW/√Hz), the nonlinearity χ , and the sensitivity γ (in V⁻¹), defined as follows:

$$NEP = \sqrt{4k_B TR_{D0}} / \beta \quad (8)$$

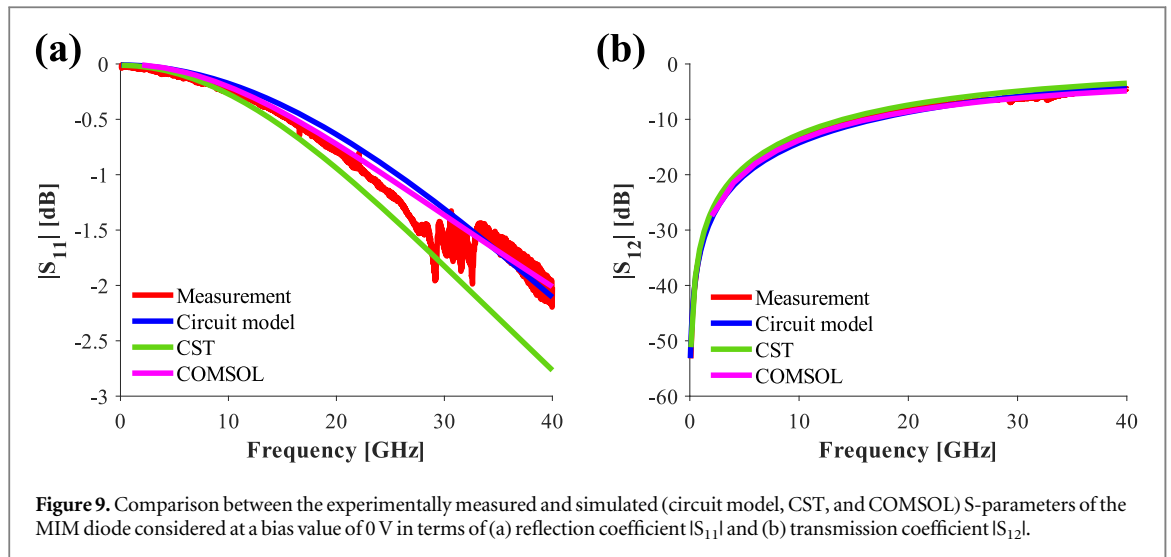
$$\chi = (\partial I / \partial V) / (I / V) \quad (9)$$

$$\gamma = (\partial^2 I / \partial V^2) / (\partial I / \partial V) \quad (10)$$

In (8), k_B is Boltzmann's constant, T is the temperature, $R_{D0} = R_D(V = 0)$ is the differential resistance R_D (in Ω) at 0 V, and β is the responsivity. In figure 8 we plot the NEP (figure 8(a)), χ (figure 8(b)), and γ (figure 8(c)) as extracted from the DC measurements. We can observe the following: (i) the maximum NEP is less than 200 pW/√Hz, which is a very low value; (ii) $\chi_{\max} \geq 4$; (iii) the maximum sensitivity is $\gamma_{\max} \approx 25$ V⁻¹, an excellent value beyond the actual state-of-the-art. These results make the proposed HfO₂-based MIM device an ideal candidate for microwave sensing/energy-harvesting in wireless systems.

The microwave characterisation of the fabricated MIM diodes integrated on CPW lines was carried out by using a vector network analyser (VNA, Anritsu 37397D) connected to a probe station (SÜSS MicroTec) with ground-signal-ground (GSG) probe tips. The S-parameter measurements were performed by using a standard short-open-load-thru (SOLT) calibration to de-embed the effects of cables, connectors, and CPW probe tips in a large band up to 40 GHz (measurements at higher frequencies were not possible due to limitations in the setup), with an input power level less than -20 dBm to operate in small-signal regime and, hence, to avoid nonlinear effects in the extraction of the S-parameters (i.e., reflection (S_{11}) and transmission (S_{12}) coefficients).

Figure 9 shows the comparison between the experimental results and the EM modelling by using a circuit model, CST, and COMSOL; theoretical and simulated data were considered at 0 V bias. As reported in figure 9, the comparisons are in excellent agreement: in fact, all the results are within 0.5 dB (i.e., the fluctuations around 30 GHz in figure 9(a) and due to small calibration errors) from the experimental data, which have been collected



up to 40 GHz to cover the whole microwave spectrum and part of the millimetre-wave frequency range. The outcomes are even more remarkable if we consider that simulating such a structure with any finite-element method (FEM, for COMSOL) or finite-integration technique (FIT, for CST) is extremely difficult without the proper numerical strategy, as the aspect ratio between the minimum dimension (oxide's thickness) and the maximum one (overall length of the CPW line with the integrated MIM device) is 1:201,428, which can create insurmountable difficulties in the mesh cell discretization of the used 3D-EM tool. The results were not affected even by changing the bias of the diode, demonstrating the very low influence of the differential resistance of the MIM diode, compared with the capacitive effect.

It is also possible to estimate the cut-off frequency f_c of the proposed HfO₂-based MIM device: using an approach similar to the one in [48], we can write $f_c = 1/(2\pi RC)$, where R attains values between 1 and 10 Ω and is the maximum (estimated) resistance of the lead lines (i.e., the CPW pads), and C the contact area's capacitance. With this data, f_c is between 460 GHz and 4.6 THz. Hence, the proposed HfO₂-based MIM diode is suitable for applications well beyond the millimetre-wave range for detection and energy-harvesting applications.

4. Conclusion

In this paper, we have presented a comprehensive study of a metal-insulator-metal (MIM) diode composed of platinum as source electrode, titanium as drain electrode, and a monoclinic hafnia layer as dielectric material between the metals, with a thickness smaller than 4 nm and a contact area of 4 μm^2 . The proposed MIM device operation is based on quantum tunnelling, and *ab initio* simulations were performed in order to obtain an overview of the optical and electronic properties of HfO₂. The geometry obtained from the optimisation of the structure is shown, together with the respective projected density of the electronic states, band structure, and dielectric constant as functions of energy. The interface between the dielectric and both metals was optimised, and the current–voltage characteristics of the resulting device estimated by means of DFT calculations by biasing the MIM diode in the voltage range between -1 V and $+1$ V. Also, the dielectric parameters resulting from the *ab initio* calculations were used to evaluate the performance from a circuit and electromagnetic point of view; in particular, the high-frequency behavior of the device up to 60 GHz was investigated by using a circuit model, as well as the CST, and COMSOL algorithms. To corroborate the multilevel modelling, the MIM device was manufactured and experimentally characterised. The I–V characteristics, as well as the scattering parameters computed with both circuit and electromagnetic simulations match almost perfectly the experimental data up to 40 GHz.

The key point of the proposed approach is the use of *ab initio* simulations to transfer and integrate the information into the circuit/electromagnetic modelling, thus confirming the correctness of the multilevel simulation platform and bypassing the conundrum of translating nanoscale phenomena into meso- and macroscale observations. As far as the authors know, this is the first model to simulate MIM diodes through the integration of atomistic- with mesoscale-level computational tools. In fact, from the atomistic (*ab initio*) simulations of hafnium oxide, we derived equivalent constitutive relations/parameters (conductivity, permittivity, losses, etc) to be inserted in multiscale full-wave modeling. Moreover, this study offers deep insights into DFT methods and atomistic simulations applied to real MIM diodes.











Acknowledgments

This work was supported by the European Project H2020 FETPROACT-EIC-05-2019 ‘NANO-EH’ under GA No. 951761, and by the Romanian Ministry of Research, Innovation and Digitization, CNCS-UEFISCDI, project number PN-III-P4-PCE-2021-0223. The authors would like to acknowledge CINECA-HPC ISCRA MARCONI-100 computer system (ATOM-HMV project n. HP10CEE3EH) for the calculations on Quantum Espresso. The authors want to thank Dr George Deligeorgis from FORTH-IESL, Heraklion, Greece for the fabrication.

Data availability statement

The data cannot be made publicly available upon publication because no suitable repository exists for hosting data in this field of study. The data that support the findings of this study are available upon reasonable request from the authors.

ORCID iDs

Eleonora Pavoni  <https://orcid.org/0000-0002-0711-0021>
Emiliano Laudadio  <https://orcid.org/0000-0002-8053-6539>
Christopher Hardly Joseph  <https://orcid.org/0000-0003-0251-5975>
Gian Marco Zampa  <https://orcid.org/0000-0002-9957-8691>
Paola Russo  <https://orcid.org/0000-0002-9015-1464>
Davide Mencarelli  <https://orcid.org/0000-0002-3380-5839>
Mircea Dragoman  <https://orcid.org/0000-0001-6886-5295>
Pierluigi Stipa  <https://orcid.org/0000-0001-9024-0398>
Luca Pierantoni  <https://orcid.org/0000-0002-2536-7613>
Martino Aldrigo  <https://orcid.org/0000-0003-2257-1966>

References

- [1] Salter T, Metzger G and Goldsman N 2009 Parasitic aware optimization of an RF power scavenging circuit with applications to smartdust sensor networks in *IEEE Radio and Wireless Symposium* **2009** 332–5
- [2] Ladan S and Wu K 2013 High efficiency low-power microwave rectifier for wireless energy harvesting in *IEEE MTT-S International Microwave Symposium Digest (MTT)* **2013** 1–4
- [3] Boreman G D 2004 Antenna-coupled metal-oxide-metal diodes for dual-band detection at 92.5 GHz and 28 THz *Electron. Lett.* **40** 116–8
- [4] Grover S and Moddel G 2011 Applicability of metal/insulator/metal (MIM) diodes to solar rectennas *IEEE J. Photovolt.* **1** 78–83
- [5] Bareiß M, Weiler B, Kälblein D, Zschieschang U, Klauk H, Scarpa G, Fabel B, Lugli P and Porod W 2012 Nano-transfer printing of functioning MIM tunnel diodes in *IEEE Silicon Nanoelectronics Workshop (SNW)* **2012** 1–2
- [6] Simmons J G 1964 Potential barriers and emission-limited current flow between closely spaced parallel metal electrodes *J. Appl. Phys.* **35** 2472–81
- [7] Ajayi O A 2014 DC and RF characterization of high frequency ALD enhanced nanostructured metal-insulator-metal diodes nanostructured metal-insulator-metal diodes *USF Tampa Graduate Theses and Dissertations*. **1** 1–172 (<https://digitalcommons.usf.edu/etd>) accessed July 10, 2023
- [8] Dudek P, Schmidt R, Lukosius M, Lupina G, Wenger C, Abrutis A, Albert M, Xu K and Devi A 2011 Basic investigation of HfO₂ based metal-insulator-metal diodes in: *Thin Solid Films* 5796–9
- [9] El Kamel F, Gonon P, Vallée C and Jorel C 2009 Electrode effects on the conduction mechanisms in HfO₂-based metal-insulator-metal capacitors *J. Appl. Phys.* **106** 064508
- [10] Mitrovic I Z, Almalki S, Tekin S B, Sedghi N, Chalker P R and Hall S 2021 Oxides for rectenna technology *Materials*. **14** 5218
- [11] Pavoni E, Mohebbi E, Mencarelli D, Stipa P, Laudadio E and Pierantoni L 2022 The effect of Y doping on monoclinic, orthorhombic, and cubic polymorphs of HfO₂: a first principles study *Nanomaterials*. **12** 4324
- [12] Zhou D, Müller J, Xu J, Knebel S, Bräuhäus D and Schröder U 2012 Insights into electrical characteristics of silicon doped hafnium oxide ferroelectric thin films *Appl. Phys. Lett.* **100** 082905–12
- [13] Robertson J 2006 High dielectric constant gate oxides for metal oxide Si transistors *Rep. Prog. Phys.* **69** 327–96
- [14] Dragoman M, Modreanu M, Povey I M, Dinescu A, Dragoman D, Di Donato A, Pavoni E and Farina M 2018 Wafer-scale very large memory windows in graphene monolayer/HfZrO ferroelectric capacitors *Nanotechnology* **29** 425204
- [15] Pavoni E, Mohebbi E, Stipa P, Mencarelli D, Pierantoni L and Laudadio E 2022 The Role of Zr on monoclinic and orthorhombic Hf Zry O₂ systems: a first-principles study *Materials*. **15** 4175–88
- [16] Laudadio E, Stipa P, Pierantoni L and Mencarelli D 2022 Phase properties of different HfO₂ polymorphs: a DFT-based study *Crystals (Basel)*. **12** 90
- [17] Schlom D G and Haeni J H 2002 A thermodynamic approach to selecting alternative gate dielectrics *MRS Bull.* **27** 198–204
- [18] Pavoni E, Mohebbi E, Stipa P, Pierantoni L, Mencarelli D, Dragoman M, Aldrigo M and Laudadio E 2023 First-principles investigation of interface phenomena in hafnium-based metal-insulator-metal diodes *Nanoscale Adv.* **5** 2748–55
- [19] Al-Dirini F, Hossain F M, Nirmalathas A and Skafidas E 2014 All-graphene planar self-switching MISFEDs, metal-insulator-semiconductor field-effect diodes *Sci. Rep.* **4** 3983

- [20] Kang J, Liu W, Sarkar D, Jena D and Banerjee K 2014 Computational study of metal contacts to monolayer transition-metal dichalcogenide semiconductors *Phys Rev X*. **4** 031005
- [21] Gong C, Colombo L, Wallace R M and Cho K 2014 The unusual mechanism of partial fermi level pinning at metal-MoS₂ interfaces *Nano Lett.* **14** 1714–20
- [22] Yoshizawa K, Tada T and Staykov A 2008 Orbital views of the electron transport in molecular devices *J. Am. Chem. Soc.* **130** 9406–13
- [23] Ondračka P, Holec D, Nečas D and Zajíčková L 2016 Accurate prediction of band gaps and optical properties of HfO₂ *J. Phys. D: Appl. Phys.* **49** 395301
- [24] Pavoni E, Modreanu M G, Mohebbi E, Mencarelli D, Stipa P, Laudadio E and Pierantoni L 2023 First-principles calculation of MoO₂ and MoO₃ electronic and optical properties compared with experimental data *Nanomaterials*. **13** 1319
- [25] Grimme S, Antony J, Ehrlich S and Krieg H 2010 A consistent and accurate *ab initio* parametrization of density functional dispersion correction (DFT-D) for the 94 elements H–Pu *J. Chem. Phys.* **132** 154104
- [26] Su D, Dou S and Wang G 2015 Gold nanocrystals with variable index facets as highly effective cathode catalysts for lithium–oxygen batteries *NPG Asia Mater.* **7** e155–155
- [27] Santos V P and Camara G A 2021 Platinum single crystal electrodes: prediction of the surface structures of low and high miller indexes faces *Results in Surfaces and Interfaces*. **3** 100006
- [28] Aldrigo M, Dragoman M, Iordanescu S, Shanawani M A and Deligeorgis G 2022 Microwave sensing using metal-insulator-metal diodes based on 4-nm-thick hafnium oxide in 2021 *16th European Microwave Integrated Circuits Conference (EuMIC)* (IEEE) **370–3**
- [29] Smidstrup S et al 2019 QuantumATK: an integrated platform of electronic and atomic-scale modelling tools *J. Phys. Condens. Matter* **32** 015901
- [30] Wan Z, Wang Q-D, Liu D and Liang J 2021 Effectively improving the accuracy of PBE functional in calculating the solid band gap via machine learning *Comput. Mater. Sci.* **198** 110699
- [31] Perdew J P, Burke K and Ernzerhof M 1996 Generalized gradient approximation made simple *Phys. Rev. Lett.* **78** 1396
- [32] van Setten M J, Giantomassi M, Bousquet E, Verstraete M J, Hamann D R, Gonze X and Rignanese G-M 2018 The pseudodojo: training and grading a 85 element optimized norm-conserving pseudopotential table *Comput. Phys. Commun.* **226** 39–54
- [33] Mohebbi E, Pavoni E, Mencarelli D, Stipa P, Pierantoni L and Laudadio E 2022 Insights into first-principles characterization of the monoclinic VO₂(B) polymorph via DFT + U calculation: electronic, magnetic and optical properties *Nanoscale Adv.* **4** 3634–46
- [34] Giannozzi P et al 2017 Advanced capabilities for materials modelling with quantum ESPRESSO *J. Phys. Condens. Matter* **29** 32
- [35] Soler J M, Artacho E, Gale J D, García A, Junquera J, Ordejón P and Sánchez-Portal D 2002 The siesta method for *ab initio* order-N materials simulation *J. Phys.: Condens. Matter* **14** 2745
- [36] Shilpi K, Bhatt S, Kumar S and Tripathi C C 2017 A study on design aspects of MIM diodes for high frequency applications *2017 2nd International Conference for Convergence in Technology I2CT 2017* **2017** 738–41
- [37] Kaur A and Chahal P 2018 RF characterization of NiO and TiO₂ based metal-insulator-metal (MIM) diodes on flexible substrates *IEEE Access*. **6** 55653–60
- [38] Monaghan S, Hurlley P K, Cherkaoui K, Negara M A and Schenk A 2009 Determination of electron effective mass and electron affinity in HfO₂ using MOS and MOSFET structures *Solid State Electron.* **53** 438–44
- [39] Zheng W, Bowen K H, Li J, Dąbkowska I and Gutowski M 2005 Electronic structure differences in ZrO₂ vs HfO₂ *J. Phys. Chem. A* **109** 11521–5
- [40] Adams D M, Leonard S, Russell D R and Cernik R J 1991 X-ray diffraction study of hafnia under high pressure using synchrotron radiation *J. Phys. Chem. Solids* **52** 1181–6
- [41] Muhammadiyah S, Suryana Y K, Azizah N and Darma Y 2019 The effect of co-existing cations on optical conductivity and absorption in Hf_{0.5}Zr_{0.5}O₂ system: a first-principles study in *J. Phys. Conf. Ser.* (Institute of Physics Publishing)
- [42] Lim S G, Kriventsov S, Jackson T N, Haeni J H, Schlom D G, Balbashov A M, Uecker R, Reiche P, Freeouf J L and Lucovsky G 2002 Dielectric functions and optical bandgaps of high- κ dielectrics for metal-oxide-semiconductor field-effect transistors by far ultraviolet spectroscopic ellipsometry *J. Appl. Phys.* **91** 4500–5
- [43] Balog M, Schieber M, Michman M and Patai S 1977 Chemical vapor deposition and characterization of HfO₂ films from organo-hafnium compounds *Thin Solid Films* **41** 247–59
- [44] Basel S, Numan N H, Khalid F G and Fakhri M A 2020 Structure and optical properties of HfO₂ nano films grown by PLD for optoelectronic device *AIP Conf Proc.* **2213** 020228
- [45] Natori K, Otani D and Sano N 1998 Thickness dependence of the effective dielectric constant in a thin film capacitor *Appl. Phys. Lett.* **73** 632–4
- [46] Gilmer D C et al 2002 Compatibility of polycrystalline silicon gate deposition with HfO₂ and Al₂O₃/HfO₂ gate dielectrics *Appl. Phys. Lett.* **81** 1288–90
- [47] Golosov D A, Vilya N, Zavadski S, Melnikov S N, Avramchuk A V, Grekhov M M, Kargin N I and Komissarov I V 2019 Influence of film thickness on the dielectric characteristics of hafnium oxide layers *Thin Solid Films* **690** 137517
- [48] Bareiß M et al 2012 High-yield transfer printing of metal-insulator-metal nanodiodes *ACS Nano*. **6** 2853–9